

Momentum transfer from the DART mission kinetic impact on asteroid Dimorphos

<https://doi.org/10.1038/s41586-023-05878-z>

Received: 2 December 2022

Accepted: 22 February 2023

Published online: 1 March 2023

Open access

 Check for updates

Andrew F. Cheng^{1✉}, Harrison F. Agrusa², Brent W. Barbee³, Alex J. Meyer⁴, Tony L. Farnham², Sabina D. Raducan⁵, Derek C. Richardson², Elisabetta Dotto⁶, Angelo Zinzi^{7,8}, Vincenzo Della Corte⁹, Thomas S. Statler¹⁰, Steven Chesley¹¹, Shantanu P. Naidu¹¹, Masatoshi Hirabayashi¹², Jian-Yang Li¹³, Siegfried Eggler¹⁴, Olivier S. Barnouin¹, Nancy L. Chabot¹, Sidney Chocron¹⁵, Gareth S. Collins¹⁶, R. Terik Daly¹, Thomas M. Davison¹⁶, Mallory E. DeCoster¹, Carolyn M. Ernst¹, Fabio Ferrari¹⁷, Dawn M. Graninger¹, Seth A. Jacobson¹⁸, Martin Jutzi⁵, Kathryn M. Kumamoto¹⁹, Robert Luther²⁰, Joshua R. Lyzhoft³, Patrick Michel²¹, Naomi Murdoch²², Ryota Nakano¹¹, Eric Palmer¹², Andrew S. Rivkin¹, Daniel J. Scheeres⁴, Angela M. Stickle¹, Jessica M. Sunshine², Josep M. Trigo-Rodriguez²³, Jean-Baptiste Vincent²⁴, James D. Walker¹⁴, Kai Wünnemann^{20,25}, Yun Zhang²⁶, Marilena Amoroso⁸, Ivano Bertini^{27,28}, John R. Brucato²⁹, Andrea Capannolo³⁰, Gabriele Cremonese³¹, Massimo Dall'Ora³², Prasanna J. D. Deshapriya⁵, Igor Gai³³, Pedro H. Hasselmann⁶, Simone Ieva⁶, Gabriele Impresario⁸, Stavro L. Ivanovski³⁴, Michèle Lavagna¹⁷, Alice Lucchetti³¹, Elena M. Epifani⁶, Dario Modenini³³, Maurizio Pajola³¹, Pasquale Palumbo²⁷, Davide Perna⁶, Simone Pirrotta⁸, Giovanni Poggiali²⁹, Alessandro Rossi³⁵, Paolo Tortora³³, Marco Zannoni³³ & Giovanni Zanotti¹⁷

The NASA Double Asteroid Redirection Test (DART) mission performed a kinetic impact on asteroid Dimorphos, the satellite of the binary asteroid (65803) Didymos, at 23:14 UTC on 26 September 2022 as a planetary defence test¹. DART was the first hypervelocity impact experiment on an asteroid at size and velocity scales relevant to planetary defence, intended to validate kinetic impact as a means of asteroid deflection. Here we report a determination of the momentum transferred to an asteroid by kinetic impact. On the basis of the change in the binary orbit period², we find an instantaneous reduction in Dimorphos's along-track orbital velocity component of $2.70 \pm 0.10 \text{ mm s}^{-1}$, indicating enhanced momentum transfer due to recoil from ejecta streams produced by the impact^{3,4}. For a Dimorphos bulk density range of $1,500$ to $3,300 \text{ kg m}^{-3}$, we find that the expected value of the momentum enhancement factor, β , ranges between 2.2 and 4.9, depending on the mass of Dimorphos. If Dimorphos and Didymos are assumed to have equal densities of $2,400 \text{ kg m}^{-3}$, $\beta = 3.6^{+0.19}_{-0.25} (1\sigma)$. These β values indicate that substantially more momentum was transferred to Dimorphos from the escaping impact ejecta than was incident with DART. Therefore, the DART kinetic impact was highly effective in deflecting the asteroid Dimorphos.

Observations from the NASA Double Asteroid Redirection Test (DART) spacecraft on approach found Dimorphos to be an oblate spheroid with a boulder-strewn surface, and the spacecraft struck within 25 m of the centre of the figure¹. Ejecta from the DART impact were observed in situ by the Italian Space Agency's Light Italian Cubesat for Imaging of Asteroids (LICIACube) spacecraft, which performed a flyby of Dimorphos with a closest approach about 168 s after the DART impact⁵. The impact ejecta were further observed by Earth- and space-based telescopes, revealing ejecta streams and dust tails similar to those seen in active asteroids thought to be triggered by natural impacts^{3,6}. Ground-based telescopes and radar determined that the DART impact reduced the binary orbit period by $33.0 \pm 1.0 (3\sigma) \text{ min}$ (ref. 2).

As a planetary defence test mission, a key objective of DART is to determine the amount of momentum transferred to the target body relative to the incident momentum of the spacecraft, quantified by the momentum enhancement factor β (for example, refs. 4,7,8), which is defined by the momentum balance of the kinetic impact,

$$M\Delta\mathbf{v} = m\mathbf{U} + m(\beta - 1)(\hat{\mathbf{E}} \cdot \mathbf{U})\hat{\mathbf{E}}. \quad (1)$$

Here, M is the mass of Dimorphos, $\Delta\mathbf{v}$ is the impact-induced change in Dimorphos's orbital velocity, m is DART's mass at impact, \mathbf{U} is DART's velocity relative to Dimorphos at impact and $\hat{\mathbf{E}}$ is the net ejecta momentum direction. $M\Delta\mathbf{v}$ is the momentum transferred to Dimorphos, $m\mathbf{U}$ is DART's incident momentum and the final term in the equation is the

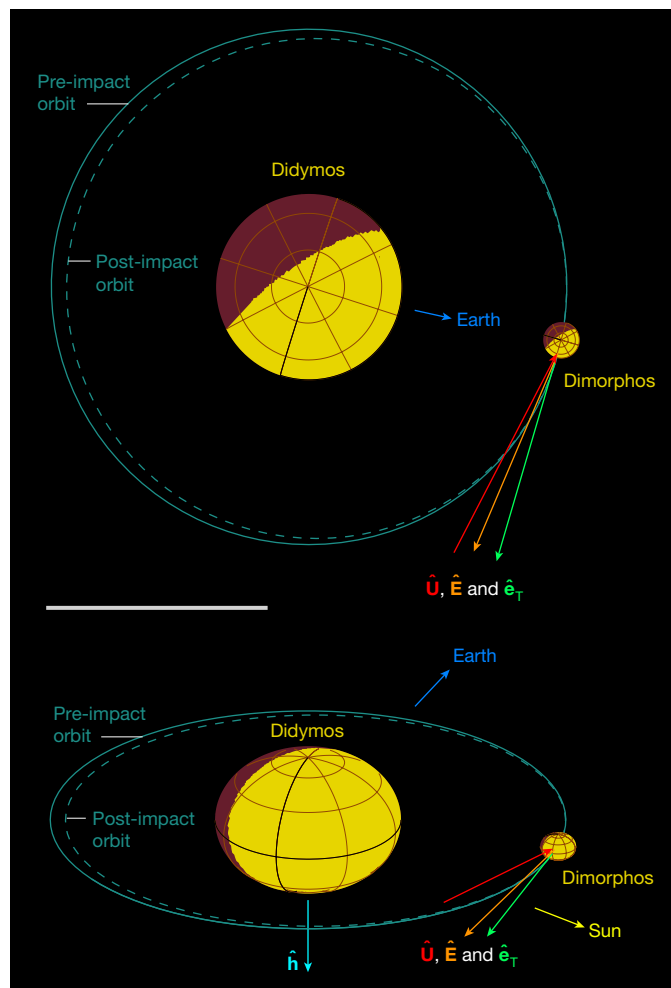


Fig. 1 | Schematic of the DART impact geometry on Dimorphos. The pre-impact orbit is shown with a solid line around Didymos. The dashed line sketches the orbit change due to the impact. Orbits are drawn roughly to scale. The positive pole direction of Didymos is \hat{h} (pointing down in the bottom panel). DART's incident direction is \hat{U} , the net ejecta momentum direction is \hat{E} (which points to a right ascension (RA) and declination (Dec) of 138° and $+13^\circ$, respectively), and the direction of Dimorphos's orbital motion, referred to as the along-track direction, is \hat{e}_T . The relative positions of the Sun and the Earth are also indicated. The upper panel shows the view from Didymos's negative pole direction, whereas the lower panel provides a perspective view. Scale bar, 1 km.

ejecta's net momentum written in terms of the spacecraft incident momentum. In this formulation, β is the ratio of actual imparted momentum to the impactor's momentum in the direction of the net ejecta momentum. Although previous works have defined β using the impactor's momentum in the surface normal direction^{8,9}, we elect to use the ejecta direction instead as our reference for the result to be independent of the surface topography. These definitions are equivalent in the case in which the ejecta direction is in the surface normal direction. A β value near 1 would indicate that ejecta recoil had made only a negligible contribution to the momentum transfer. A $\beta > 2$ would mean that the ejecta momentum contribution exceeded the incident momentum from DART.

The full Δv cannot be determined with the available information¹⁰, but its component along Dimorphos's orbital velocity direction, referred to as the along-track direction, can be estimated from available data including Dimorphos's orbit period change. To express β in terms of the along-track component of Δv , we take the scalar product of (1) with the unit vector \hat{e}_T in the along-track direction. Solving for β yields,

$$\beta = 1 + \frac{M}{m} \frac{(\Delta v \cdot \hat{e}_T) - (U \cdot \hat{e}_T)}{(\hat{E} \cdot U)(\hat{E} \cdot \hat{e}_T)} \quad (2)$$

For the remainder of this work, we refer to the along-track component of Dimorphos's velocity change, $\Delta v \cdot \hat{e}_T$, as Δv_T . Figure 1 shows the geometry of the DART impact, including the nominal ellipsoidal shapes used for Didymos and Dimorphos in our analysis, and the nominal orientations of U , \hat{e}_T and \hat{E} at the time of impact.

The major unknowns in calculating β are Δv_T , M and \hat{E} . We first use a Monte Carlo approach to produce a distribution for Δv_T consistent with the measured period change that incorporates the various uncertainties involved. We sample many possible combinations of Didymos system parameters, including the ellipsoid shape extents of the asteroids, pre-impact orbit separation distance between the two asteroids' centres of mass (that is, Dimorphos's pre-impact orbit radius), pre- and post-impact orbit periods, and net ejecta momentum direction \hat{E} . We use the full two-body problem code (General Use Binary Asteroid Simulator (GUBAS)¹¹, Methods) that implements coupled rotational and orbital dynamics to numerically determine Δv_T for each sampled combination of input parameters. Coupled dynamics are necessary because of the non-spherical shapes of Didymos and Dimorphos and their close proximity relative to their sizes. A range of values for M is generated by combining the volumes of the sampled ellipsoid shape parameters with values for Dimorphos's density. The Monte Carlo approach is summarized by Extended Data Fig. 1. As Dimorphos's density has not been directly measured and has a large uncertainty, we treat it as an independent variable and uniformly sample a wide range of possible values between $1,500$ and $3,300 \text{ kg m}^{-3}$, a range that encompasses the 3σ uncertainty¹. Using a technique modified from that of ref. 12 (Methods), we apply observations of the ejecta by means of Hubble and LICIAcube data to obtain a preliminary measurement of the axis of the ejecta cone geometry (Extended Data Figs. 2 and 3). The cone axis direction is identical to \hat{E} assuming the ejecta plume holds the momentum uniformly, and we find \hat{E} points towards a right ascension and declination (Dec) of 138° and $+13^\circ$, respectively (Extended Data Fig. 2). We assign a conservative uncertainty of 15° around this direction. Finally, β also depends on DART's mass and impact velocity, as well as Didymos's pole orientation². Those quantities have negligibly small uncertainties relative to those of the other parameters discussed previously and are therefore treated as fixed values (not sampled). See Methods for additional details on the Monte Carlo analysis, Extended Data Table 1 for a list of parameters and uncertainties, and Extended Data Table 2 for the covariances that were used.

We find that $\Delta v_T = -2.70 \pm 0.10$ (1σ) mm s^{-1} , on the basis of the observed impact-induced period change of -33.0 ± 1.0 (3σ) minutes and the shapes and separation of Didymos and Dimorphos^{1,2}. Figure 2 shows the distribution of Δv_T values from the Monte Carlo analysis, along with the fitted mean and standard deviation. The resulting spread of β values as a function of Dimorphos's density, calculated by means of equation (2), is presented in Fig. 3, along with linear fits for the mean β versus density trend and its 1σ confidence intervals. The linear-fit slope is expressed as a scale factor on the ratio of density to the nominal value of $2,400 \text{ kg m}^{-3}$ (ref. 1). For that nominal Dimorphos density, at which Dimorphos and Didymos would have roughly equal densities, $\beta = 3.61^{+0.19}_{-0.25}$ with 1σ confidence. The mean β ranges between 2.2 and 4.9 as a function of density across the range of $1,500$ to $3,300 \text{ kg m}^{-3}$ and, overall, β ranges between 1.9 and 5.5 with 3σ confidence.

Our result for β is consistent with numerical simulations^{13–23} and laboratory experiments^{24–29} of kinetic impacts, which have consistently indicated that β is expected to fall between about 1 and 6. However, non-unique combinations of asteroid mechanical properties (for example, cohesive strength, porosity and friction angle) can

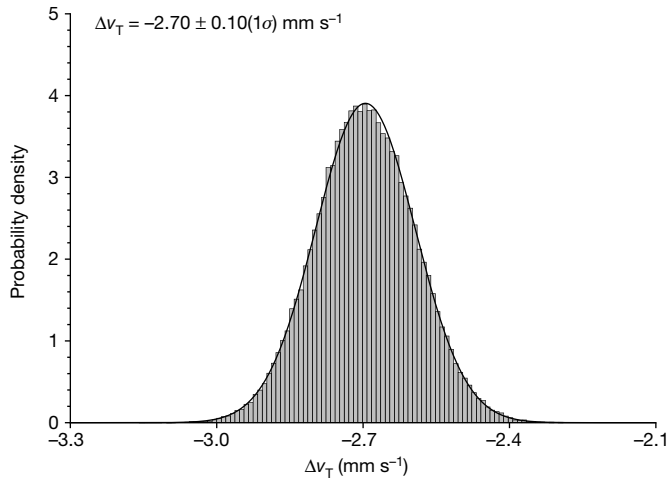


Fig. 2 | Probability distribution of Δv_T , the along-track component of the change in Dimorphos's velocity induced by DART's impact, generated by our Monte Carlo analysis that samples over input parameter uncertainties. The histogram consists of 100,000 Monte Carlo samples and is normalized to an area of unity. A Gaussian fit to the distribution indicates a mean Δv_T of -2.70 mm s^{-1} with a standard deviation of 0.10 mm s^{-1} .

produce similar values of β in impact simulations²⁰. Future studies that combine estimates of β with additional constraints from the DART impact site geology¹ and ejecta observations^{3,5} will provide greater insight into Dimorphos's material properties. In addition, ESA's Hera mission³⁰ is planned to arrive at the Didymos system in late 2026. By measuring Dimorphos's mass and other orbital properties, Hera will allow us to significantly improve the accuracy and precision of the β determination.

DART's impact demonstrates that the momentum transfer to a target asteroid can substantially exceed the incident momentum of the

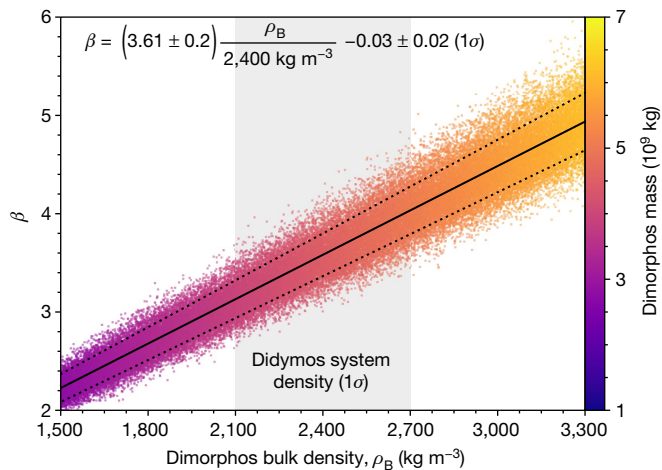


Fig. 3 | β as a function of Dimorphos's bulk density ρ_B , from the dynamical Monte Carlo analysis. Individual samples are plotted as points, whereas the linear fit for the mean β is plotted as the solid line and the dotted lines show the 1σ confidence interval. The colour bar indicates the mass of Dimorphos corresponding to each Monte Carlo sample, which is determined by bulk density and the volume. The density range shown corresponds to the 3σ range of the Didymos system density, whereas the shaded region highlights the 1σ range¹. If the density of Dimorphos were $2,400 \text{ kg m}^{-3}$, the densities of Didymos and Dimorphos would be the same as the system density, and $\beta = 3.61^{+0.19}_{-0.25} (1\sigma)$. For context, the densities of three other S-type near-Earth asteroids are in the ranges shown: 433 Eros^{32} at $2,670 \pm 30 \text{ kg m}^{-3}$; $25143 \text{ Itokawa}^{33}$ at $1,900 \pm 130 \text{ kg m}^{-3}$ and $66391 \text{ Moshup}^{34}$ at $1,970 \pm 240 \text{ kg m}^{-3}$.

kinetic impactor, validating the effectiveness of kinetic impact for preventing future asteroid strikes on the Earth. The value of β from a kinetic impact is key to informing the strategy of a kinetic impactor mission (or missions) to mitigate a future asteroid impact threat to Earth³¹. Should β turn out to be greater than two across a wide range of asteroid types, it would mean important performance improvements for kinetic impactor asteroid deflection missions. If $\beta > 2$, as opposed to $\beta \cong 1$, then the same sized kinetic impactor could deflect a given asteroid with less warning time, or deflect a larger asteroid with a given warning time than it otherwise could.

Online content

Any methods, additional references, Nature Portfolio reporting summaries, source data, extended data, supplementary information, acknowledgements, peer review information; details of author contributions and competing interests; and statements of data and code availability are available at <https://doi.org/10.1038/s41586-023-05878-z>.

- Daly, R. T. et al. Successful kinetic impact into an asteroid for planetary defence. *Nature* <https://doi.org/10.1038/s41586-023-05810-5> (2023).
- Thomas, C. A. et al. Orbital period change of Dimorphos due to the DART kinetic impact. *Nature* <https://doi.org/10.1038/s41586-023-05805-2> (2023).
- Li, J.-Y. et al. Ejecta from the DART-produced active asteroid Dimorphos. *Nature* <https://doi.org/10.1038/s41586-023-05811-4> (2023).
- Ahrens, T. J. & Harris, A. W. in *Hazards Due to Comets and Asteroids* 897–927 (Univ. of Arizona Press, 1994).
- Dotto, E. et al. LICIACube—The Light Italian Cubesat for imaging of asteroids in support of the NASA DART mission towards asteroid (65803) Didymos. *Planet. Space Sci.* **199**, 105185 (2021).
- Tancredi, G., Liu, P.-Y., Campo-Bagatin, A., Moreno, F. & Dominguez, B. Lofting of low speed ejecta produced in the DART experiment and production of a dust cloud. *Mon. Not. R. Astron. Soc.* <https://doi.org/10.1093/mnras/stac3258> (2022).
- Holsapple, K. A. & Housen, K. R. Momentum transfer in asteroid impacts. I. Theory and scaling. *Icarus* **221**, 875–887 (2012).
- Rivkin, A. S. et al. The Double Asteroid Redirection Test (DART): planetary defense investigations and requirements. *Planet. Sci. J.* **2**, 173 (2021).
- Feldhacker, J. D. et al. Shape dependence of the kinetic deflection of asteroids. *J. Guid. Control Dyn.* **40**, 2417–2431 (2017).
- Richardson, D. C. et al. Predictions for the dynamical states of the Didymos system before and after the planned DART impact. *Planet. Sci. J.* **3**, 157 (2022).
- Davis, A. B. & Scheeres, D. J. Doubly synchronous binary asteroid mass parameter observability. *Icarus* **341**, 113439 (2020).
- Farnham, T. L. & Cochran, A. L. A McDonald Observatory study of comet 19P/Borrelly: placing the deep space 1 observations into a broader context. *Icarus* **160**, 398–418 (2002).
- Jutzi, M. & Michel, P. Hypervelocity impacts on asteroids and momentum transfer. I. Numerical simulations using porous targets. *Icarus* **229**, 247–253 (2014).
- Bruck Syal, M., Michael Owen, J. & Miller, P. L. Deflection by kinetic impact: sensitivity to asteroid properties. *Icarus* **269**, 50–61 (2016).
- Cheng, A. F. et al. Asteroid impact & deflection assessment mission: kinetic impactor. *Planet. Space Sci.* **121**, 27–35 (2016).
- Raducan, S. D., Davison, T. M., Luther, R. & Collins, G. S. The role of asteroid strength, porosity and internal friction in impact momentum transfer. *Icarus* **329**, 282–295 (2019).
- Raducan, S. D., Davison, T. M. & Collins, G. S. The effects of asteroid layering on ejecta mass-velocity distribution and implications for impact momentum transfer. *Planet. Space Sci.* **180**, 104756 (2020).
- Rainey, E. S. G. et al. Impact modeling for the Double Asteroid Redirection Test (DART) mission. *Int. J. Impact Eng.* **142**, 103528 (2020).
- Kumamoto, K. M. et al. Predicting asteroid material properties from a DART-like kinetic impact. *Planet. Sci. J.* **3**, 237 (2022).
- Stickley, A. M. et al. Effects of impact and target parameters on the results of a kinetic impactor: predictions for the Double Asteroid Redirection Test (DART) mission. *Planet. Sci. J.* **3**, 248 (2022).
- Owen, J. M., DeCoster, M. E., Graninger, D. M. & Raducan, S. D. Spacecraft geometry effects on kinetic impactor missions. *Planet. Sci. J.* **3**, 218 (2022).
- Luther, R. et al. Momentum enhancement during kinetic impacts in the low-intermediate-strength regime: benchmarking and validation of impact shock physics codes. *Planet. Sci. J.* **3**, 227 (2022).
- DeCoster, M. E., Rainey, E. S. G., Rosch, T. W. & Stickle, A. M. Statistical significance of mission parameters on the deflection efficiency of kinetic impacts: applications for the next-generation kinetic impactor. *Planet. Sci. J.* **3**, 186 (2022).
- Walker, J. D., Chocron, S., Grosch, D. J., Marchi, S. & Alexander, A. M. Momentum enhancement from a 3 cm diameter aluminum sphere striking a small boulder assembly at 5.4 km s^{-1} . *Planet. Sci. J.* **3**, 215 (2022).
- Flynn, G. J. et al. Hypervelocity cratering and disruption of porous pumice targets: implications for crater production, catastrophic disruption, and momentum transfer on porous asteroids. *Planet. Space Sci.* **107**, 64–76 (2015).
- Durda, D. D. et al. Laboratory impact experiments with decimeter-to-meter-scale targets to measure momentum enhancement. *Planet. Space Sci.* **178**, 104694 (2019).

27. Flynn, G. J. et al. Momentum transfer in hypervelocity cratering of meteorites and meteorite analogs: implications for orbital evolution and kinetic impact deflection of asteroids. *Int. J. Impact Eng.* **136**, 103437 (2020).
28. Hoerth, T., Schäfer, F., Hupfer, J., Millon, O. & Wickert, M. Momentum transfer in hypervelocity impact experiments on rock targets. *Procedia Eng.* **103**, 197–204 (2015).
29. Walker, J. D. et al. Momentum enhancement from aluminum striking granite and the scale size effect. *Int. J. Impact Eng.* **56**, 12–18 (2013).
30. Michel, P. et al. The ESA Hera mission: detailed characterization of the DART impact outcome and of the binary asteroid (65803) Didymos. *Planet. Sci. J.* **3**, 160 (2022).
31. Statler, T. S. et al. After DART: using the first full-scale test of a kinetic impactor to inform a future planetary defense mission. *Planet. Sci. J.* **3**, 244 (2022).
32. Yeomans, D. K. et al. Radio science results during the NEAR-Shoemaker spacecraft rendezvous with Eros. *Science* **289**, 2085–2088 (2000).
33. Fujiwara, A. et al. The rubble-pile asteroid Itokawa as observed by Hayabusa. *Science* **312**, 1330–1334 (2006).
34. Ostro, S. J. et al. Radar imaging of binary near-Earth asteroid (66391) 1999 KW4. *Science* **314**, 1276–1280 (2006).

Publisher's note Springer Nature remains neutral with regard to jurisdictional claims in published maps and institutional affiliations.



Open Access This article is licensed under a Creative Commons Attribution 4.0 International License, which permits use, sharing, adaptation, distribution and reproduction in any medium or format, as long as you give appropriate credit to the original author(s) and the source, provide a link to the Creative Commons licence, and indicate if changes were made. The images or other third party material in this article are included in the article's Creative Commons licence, unless indicated otherwise in a credit line to the material. If material is not included in the article's Creative Commons licence and your intended use is not permitted by statutory regulation or exceeds the permitted use, you will need to obtain permission directly from the copyright holder. To view a copy of this licence, visit <http://creativecommons.org/licenses/by/4.0/>.

© The Author(s) 2023

¹Applied Physics Laboratory, Johns Hopkins University, Laurel, MD, USA. ²Department of Astronomy, University of Maryland, College Park, MD, USA. ³NASA/Goddard Space Flight Center, Greenbelt, MD, USA. ⁴Smead Department of Aerospace Engineering Sciences, University of Colorado Boulder, Boulder, CO, USA. ⁵Space Research and Planetary Sciences, Physical Institute, University of Bern, Bern, Switzerland. ⁶INAF, Astronomical Observatory of Rome, Rome, Italy. ⁷Space Science Data Center (ASI), Roma, Italy. ⁸Italian Space Agency – ASI, Sede di Roma, Rome, Italy. ⁹INAF, Institute of Space Astrophysics and Planetology, Roma, Italy. ¹⁰Planetary Defense Coordination Office and Planetary Science Division, NASA Headquarters, Washington, DC, USA. ¹¹Jet Propulsion Laboratory, California Institute of Technology, Pasadena, CA, USA. ¹²Auburn University, Auburn, AL, USA. ¹³Planetary Science Institute, Tucson, AZ, USA. ¹⁴Department of Aerospace Engineering, University of Illinois at Urbana-Champaign, Champaign, IL, USA. ¹⁵Southwest Research Institute, San Antonio, TX, USA. ¹⁶Imperial College London, London, UK. ¹⁷Department of Aerospace Science and Technology, Polytechnic University of Milan, Milano, Italy. ¹⁸Michigan State University, East Lansing, MI, USA. ¹⁹Lawrence Livermore National Laboratory, Livermore, CA, USA. ²⁰Natural History Museum, Leibniz Institute for Evolution and Biodiversity Science, Berlin, Germany. ²¹Observatory of the Côte d'Azur, CNRS, Lagrange Laboratory, University of the Côte d'Azur, Nice, France. ²²Higher Institute of Aeronautics and Space (ISAE-SUPAERO), University of Toulouse, Toulouse, France. ²³Institute of Space Sciences (CSIC-IEEC), Barcelona, Spain. ²⁴DLR Institute of Planetary Research, Berlin, Germany. ²⁵Freie University of Berlin, Berlin, Germany. ²⁶Department of Aerospace Engineering, University of Maryland, College Park, MD, USA. ²⁷Department of Science and Technology, University of Naples 'Parthenope', Naples, Italy. ²⁸Institute for Space Astrophysics and Planetology (IAPS), INAF, Rome, Italy. ²⁹INAF, Astrophysical Observatory of Arcetri, Firenze, Italy. ³⁰Department of Aerospace Science and Technology (DAER), Polytechnic University of Milan, Milan, Italy. ³¹INAF, Astronomical Observatory at Padova, Padova, Italy. ³²INAF, Astronomical Observatory at Capodimonte, Napoli, Italy. ³³Department of Industrial Engineering, Alma Mater Studiorum - University of Bologna, Forlì, Italy. ³⁴INAF, Astronomical Observatory at Trieste, Trieste, Italy. ³⁵IFAC, CNR, Florence, Italy. [✉]e-mail: andy.cheng@jhuapl.edu

Methods

Numerical determination of Δv_T and β

Several parameters affect the value of β as presented in equation (2): Δv_T , M and $\hat{\mathbf{E}}$. The along-track velocity change, Δv_T depends on orbit period change, pre-impact semimajor axis and the shapes of Didymos and Dimorphos, whereas M depends on Dimorphos's shape and bulk density (which was not measured). $\hat{\mathbf{E}}$ is the only parameter that is directly observed, but it still has considerable uncertainty. Thus, there are 12 total unknown input parameters: three axis lengths for Didymos's ellipsoidal shape (A_x, A_y, A_z), three axial lengths for Dimorphos's ellipsoidal shape (B_x, B_y, B_z), Dimorphos's bulk density ρ_b , the pre-impact orbit semimajor axis a_{pre} , pre-impact orbit period P_{pre} and post-impact orbit period P_{post} , and two angles to define the ejecta momentum direction vector ($\hat{\mathbf{E}}$). Extended Data Table 1 lists these input parameter values and their uncertainties, along with additional known quantities needed to calculate β . To account for this large set of input uncertainties, we use a Monte Carlo approach in which 100,000 possible cases are generated by randomly sampling the input parameters within their uncertainties. We assume the DART spacecraft mass, DART impact velocity vector and Dimorphos's orbital velocity direction (referred to as the along-track direction) are all known precisely because their uncertainties are negligibly small compared to the uncertainties of the other input parameters.

The pre-impact orbit semimajor axis, pre-impact orbit period and post-impact orbit period are sampled as a multivariate Gaussian distribution using the mean values and covariance matrix from the 'N22+' solution (refs. 35 and 36 of ref. 2; Extended Data Tables 1 and 2). This accounts for the small correlations between those three parameters. The physical extents of Didymos and Dimorphos from ref. 1 are sampled uniformly, as those uncertainties are not Gaussian (Extended Data Table 1). β depends strongly on Dimorphos's mass, but the mass is poorly constrained because Dimorphos's bulk density has not been directly measured¹. Therefore, we treat density as the independent variable, sample it uniformly and report β as a function of Dimorphos's density.

For each Monte Carlo sample for the Didymos system, a secant search algorithm (a finite-difference Newton's method) described in ref. 37 is first used to compute the density of Didymos required to reproduce the sampled pre-impact orbit period, given the sampled pre-impact orbit semimajor axis, body shapes and Dimorphos's density. Then, a second secant search algorithm is used to determine the Δv_T required to achieve the sampled post-impact orbit period. We match the pre- and post-impact orbit periods because these are directly measured by ground-based observations and are thus the best-constrained parameters of the system². Given the non-Keplerian nature of the Didymos system, we use the GUBAS to numerically propagate the binary asteroid dynamics. GUBAS is a well-tested full two-body problem (F2BP) code that can model the mutual gravitational interactions between two arbitrarily shaped rigid bodies with uniform mass distributions^{11,38}. GUBAS has been benchmarked against other F2BP codes³⁹ and used extensively in previous dynamical studies of the Didymos system (for example, refs. 10, 37, 40). Finally, the mass of Dimorphos is calculated from its ellipsoidal shape and Dimorphos's density. This mass, along with the computed Δv_T and sampled net ejecta momentum direction, are provided as inputs to equation (2) to calculate the value of β corresponding to each of the 100,000 realizations of the system. For a discussion on estimating $\hat{\mathbf{E}}$, see the Ejecta plume direction section below. The process described herein is summarized graphically in Extended Data Fig. 1.

The convergence criteria on both secant algorithms are set such that the simulated orbit period matches the desired orbit period to an accuracy ten times better than the uncertainty on the measurements themselves. The numerical simulations measure the average orbit period of Dimorphos in an inertial frame over 30 days to account

for small fluctuations in the mutual orbit period resulting from spin-orbit coupling⁴⁰. Our selection of 100,000 as the number of samples to use in the Monte Carlo analysis was informed by calculating an estimated minimum necessary number of samples from the Central Limit Theorem and then testing sample sizes near that estimated value. The β estimate results are well converged with 100,000 samples.

In the numerical simulations, both Didymos and Dimorphos are modelled as triaxial ellipsoids with physical extents from ref. 1. Images from DRACO and LICIAcube showed that both Didymos and Dimorphos have an oblate spheroid shape¹. There is no advantage to using more sophisticated shape models while the internal mass distributions of the bodies are unknown. Instead, the ellipsoidal approximation allows for easy sampling of a range of plausible moments of inertia as a proxy for different internal density distributions. For example, given the current uncertainties in Didymos's physical extents¹, sampling over the given range of ellipsoidal shapes results in a range of plausible second-order gravity terms (analogous to the spherical harmonic terms J_2 , C_{22} and so on), which play an important role in the system's dynamics due to the tight separation of the binary components. Neglecting their shapes and assuming Keplerian dynamics results in $\Delta v_T = -2.86 \pm 0.095$ (1σ), whereas GUBAS's second-order gravity model finds $\Delta v_T = -2.70 \pm 0.10$ (1σ). Although fourth-order dynamics influence higher-order dynamical effects^{37,40}, we find that it comes with a significantly higher computational cost yet plays a negligible role in determining Δv_T . A smaller batch (due to increased computational cost) of roughly 4,000 runs was conducted with fourth-order dynamics, which resulted in $\Delta v_T = -2.68 \pm 0.10$ (1σ), indicating the second-order dynamics model is appropriate for determining Δv_T given the current uncertainties in the orbit solution and body shapes. This result was also independently verified using analytical models, accounting for Didymos's gravitational quadrupole, which agreed within a few percent of the second-order numerical results, as expected given their dynamical approximations.

We do not sample the rotation period of Dimorphos, as it is assumed to be equal to the pre-impact orbit period before the impact, with reasoning as follows. A measured orbit semimajor axis drift directed inwards⁴¹ indicates the system is evolving under the influence of the binary Yarkovsky–O'Keefe–Radzievskii–Paddack effect⁴², which requires a secondary in near-synchronous rotation. Furthermore, radar images constrain Dimorphos's spin period to be within 3 h of the synchronous rate³⁵. Recent models for tidal dissipation in binary asteroids suggest that any free libration would dissipate on 100-year timescales⁴³, making any substantial free libration unlikely given the timescales for excitation mechanisms such as close planetary encounters and natural impacts¹⁰. Furthermore, Dimorphos's pre-impact eccentricity is constrained to be less than 0.03 (refs. 35, 41), putting the maximum possible forced libration amplitude⁴⁴ at around 0.5° . Although Dimorphos's rotation state is not precisely determined by DART, this body of evidence suggests that Dimorphos was probably in near-synchronous rotation and on a nearly circular orbit before the DART impact.

Our model further assumes all momentum is transferred instantaneously, because earlier work showed the time duration of the momentum transfer has a negligible effect on the resulting dynamics¹⁰. The instantaneous torque on Dimorphos due to DART's slightly off-centre impact¹ is also neglected as the corresponding change in Dimorphos's rotation state is small compared to that arising from exciting Dimorphos's eccentricity and libration by the impact^{10, 37, 45}. Finally, the effects of reshaping and mass loss due to cratering and ejecta are also neglected, as these effects are expected to be smaller in magnitude than the current roughly 1 min uncertainty on the post-impact orbit period⁴⁶ and will remain poorly constrained until the Hera mission characterizes the Didymos system in 2027 (ref. 30). We leave these higher-order effects for future work once the post-impact orbit solution is refined further.

Ejecta plume direction

We use observations of the ejecta plume to determine the ejecta momentum direction $\hat{\mathbf{E}}$. The conical ejecta plume was imaged by the LICIAcube LUKE camera⁵ and the Hubble Space Telescope (HST)³. We apply a technique used to derive cometary spin poles¹² to estimate the orientation of the ejecta cone axis. Although it is possible to have an asymmetric distribution of ejecta momentum (mass and velocity) within the cone, we assume the cone to be axially symmetric. The approach applies the ejecta cone's bright edges (if captured in an image) to compute the apparent direction of the cone axis projected onto the sky, which is assumed to be the middle of the edges.

For a LICIAcube observation, the projected cone axis defines the LICIAcube-axis plane in inertial space that contains the line-of-sight and the projected axis. The cone axis can lie anywhere in this plane. The analogous plane HST axis is defined from early HST images of the plume (those taken within 2 h after the impact) that show similar radial velocity to the ejecta in the LICIAcube images, indicating it is probably the same ejecta material observed on a larger spatial scale. The intersection of these planes defines the cone axis orientation in three dimensions, but unfortunately the LICIAcube- and HST-axis planes are nearly parallel. Thus, these observations do not provide a unique solution but they constrain the axis orientation to a narrow swath of the sky (Extended Data Fig. 2). However, LICIAcube LUKE images resolved the ejecta cone and the cone morphology over a large range of viewing angles during the flyby, further constraining the cone axis orientation³. During the approach to Dimorphos, the cone was pointed towards LICIAcube, with the ejecta obscuring parts of Dimorphos. During recession from Dimorphos, the cone pointed away from Dimorphos and revealed it in silhouette (Extended Data Fig. 3). The tightest constraint on cone orientation would have come from closest-approach images, with the cone axis in the plane-of-sky, as the cone transitioned from pointing towards the observer to pointing away. Unfortunately, Dimorphos and the ejecta cone were outside the LUKE field of view for 13 s around closest approach, and we lack images from the transition.

The resolved LICIAcube images are used to eliminate portions of the swath in Extended Data Fig. 2 where the observed cone morphology is inconsistent with those axis orientations. For example, half of the swath is rejected because the axis would be pointed in the opposite direction of what was observed. We also exclude orientations in which the cone would point too close to the line-of-sight during the approach or recession of LICIAcube. We find the axis orientation to be (right ascension, Dec) = (138°, +13°). We assign conservative uncertainties of roughly 15° in all directions based on the angular extents of region 5 in Extended Data Fig. 2.

Data availability

The dynamical simulations were carried out using GUBAS, which is publicly available on Github (<https://github.com/meyeralexj/gubas>). The Dimorphos orbital velocity direction vector components presented in Extended Data Table 1 were computed using the `dimorphos_s501.bsp` and `sb-65803-198.bsp` (Didymos) data files available at https://dart.jhuapl.edu/SPICE_kernels/spk. The DART incident velocity vector components presented in Extended Data Table 1 were computed using those two files in combination with the `DART_2022_269_1241_ops_v01_impact.bsp` data file, available at the same URL. Data availability at that URL is planned until summer 2023, after which those data may be found at <https://naif.jpl.nasa.gov/naif/data.html>.

- Naidu, S. P. et al. Radar observations and a physical model of binary near-Earth asteroid 65803 Didymos, target of the DART mission. *Icarus* **348**, 113777 (2020).
- Naidu, S. P. et al. Anticipating the DART impact: orbit estimation of Dimorphos using a simplified model. *Planet. Sci. J.* **3**, 234 (2022).

- Agrusa, H. F. et al. The excited spin state of Dimorphos resulting from the DART impact. *Icarus* **370**, 114624 (2021).
- Hou, X., Scheeres, D. J. & Xin, X. Mutual potential between two rigid bodies with arbitrary shapes and mass distributions. *Celest. Mech. Dyn. Astron.* **127**, 369–395 (2017).
- Agrusa, H. F. et al. A benchmarking and sensitivity study of the full two-body gravitational dynamics of the DART mission target, binary asteroid 65803 Didymos. *Icarus* **349**, 113849 (2020).
- Meyer, A. J. et al. Libration-induced orbit period variations following the DART impact. *Planet. Sci. J.* **2**, 242 (2021).
- Scheirich, P. & Pravec, P. Preimpact mutual orbit of the DART target binary asteroid (65803) Didymos derived from observations of mutual events in 2003–2021. *Planet. Sci. J.* **3**, 163 (2022).
- Čuk, M. & Burns, J. A. Effects of thermal radiation on the dynamics of binary NEAs. *Icarus* **176**, 418–431 (2005).
- Meyer, A. J. et al. Energy dissipation in synchronous binary asteroids. *Icarus* **391**, 115323 (2023).
- Murray, C. D. & Dermott, S. F. *Solar System Dynamics* (Cambridge Univ. Press, 2000).
- Michel, P. et al. European component of the AIDA mission to a binary asteroid: characterization and interpretation of the impact of the DART mission. *Adv. Space Res.* **62**, 2261–2272 (2018).
- Nakano, R. et al. NASA's Double Asteroid Redirection Test (DART): mutual orbital period change due to reshaping in the near-earth binary asteroid system (65803) Didymos. *Planet. Sci. J.* **3**, 148 (2022).

Acknowledgements We thank S. Marchi, K. T. Ramesh, P. Sanchez, S. Schwartz, J. Steckloff, M. B. Syal and G. Tancredi for their comments on the manuscript. M.Z., I.G., D.M. and P.T. acknowledge D. Luby, M. Smith and D. Mages for the useful discussions and suggestions regarding the operational navigation of LICIAcube. This work was supported by the DART mission, NASA contract no. 80MSFC20D0004. S.D.R. and M.J. acknowledge support from the Swiss National Science Foundation (project number 200021_207359). S.D.R., M.J., R.L., P.M., N.M. and K.W. acknowledge the funding from the European Union's Horizon 2020 research and innovation programme, grant agreement no. 870377 (project no. NEO-MAPP). P.M. acknowledges support from CNES, ESA and the CNRS through the MITI interdisciplinary programmes. N.M. acknowledges support from CNES. E.D., V.D.C., E.M.E., A.R., I.G., P.J.D.D., P.H.H., I.B., A.Z., S.L.I., J.R.B., G.P., A.L., M.P., G.Z., M.A., A.C., G.C., M.D.O., S.I., G.I., M.L., D.M., P.P., D.P., S.P., P.T. and M.Z. acknowledge financial support from Agenzia Spaziale Italiana (ASI, contract no. 2019-31-HH.O). S.E. acknowledges support through NASA grant number 80NSSC22K1173. S.C. and J.D.W. acknowledge support from the Southwest Research Institute's internal research programme. G.S.C. and T.M.D. acknowledges support from the UK Science and Technology Facilities Council grant no. ST/S000615/1. F.F. acknowledges funding from the Swiss National Science Foundation (SNSF) Ambizione grant no. 193346. J.-Y.L. acknowledges the support provided by NASA through grant no. HST-GO-16674 from the Space Telescope Science Institute, which is operated by the Association of Universities for Research in Astronomy, Inc., under NASA contract no. NAS 5-26555, and the support from NASA DART Participating Scientist Program, grant no. 80NSSC21K1131. R.N. acknowledges support from NASA/FINESST (grant no. NNH20ZDA001N). J.M.T.-R. acknowledges financial support from project no. PID2021-128062NB-I00 funded by MCIN/AEI (Spain). Part of this research was carried out at the Jet Propulsion Laboratory, California Institute of Technology, under a contract with the National Aeronautics and Space Administration. Lawrence Livermore National Laboratory is operated by Lawrence Livermore National Security, LLC, for the US Department of Energy, National Nuclear Security Administration under contract nos. DE-AC5207NA27344 and LLNL-JRNL-84276. Simulations were performed on the YORP and ASTRA clusters administered by the Centre for Theory and Computation, part of the Department of Astronomy at the University of Maryland. M.Z., I.G., D.M. and P.T. wish to acknowledge Caltech and the Jet Propulsion Laboratory for granting the University of Bologna a license for an executable version of MONTE Project Edition S/W.

Author contributions A.F.C. led the overall conception and writing of the study. H.F.A. contributed the GUBAS dynamical simulations for the Monte Carlo analysis. B.W.B. contributed the Monte Carlo analysis. A.J.M. validated the GUBAS dynamical simulations. T.L.F. and M.H. determined the ejecta cone orientation. S.D.R. contributed to discussions of β determination and implications. A.F.C., H.F.A., B.W.B., A.J.M., T.L.F. and D.C.R. wrote most of the manuscript text. E.D. led the LICIAcube investigation as Principal Investigator. A.Z. led production of LICIAcube imaging data. V.D.C. led the calibration of the LICIAcube imagers. T.S.S. helped with verification of the GUBAS results and provided comments on the manuscript. S.C. and S.P.N. provided the Dimorphos orbital velocity vector direction, DART velocity vector at impact and the covariance matrix for the pre-impact orbit semimajor axis, mean motion and change in mean motion. J.-Y.L. helped with efforts to estimate the ejecta momentum direction from HST and LICIAcube observations. S.E., O.S.B., N.L.C., S.C., G.S.C., R.T.D., T.M.D., M.E.D., C.M.E., F.F., D.M.G., S.A.J., M.J., K.M.K., J.-Y.L., R.L., P.M., N.M., R.N., E.P., A.S.R., D.J.S., A.M.S., J.M.S., J.M.T.-R., J.-B.V., J.D.W., K.W. and Y.Z. provided useful inputs and/or comments on the manuscript. J.R.L. assisted with verification efforts for the numerical simulations. E.D., V.D.C., E.M.E., A.R., I.G., P.J.D.D., P.H.H., I.B., A.Z., S.L.I., J.R.B., G.P., A.L., M.P., G.Z., M.A., A.C., G.C., M.D.O., S.I., G.I., M.L., D.M., P.P., D.P., S.P., P.T. and M.Z. contributed to the development and operation of LICIAcube, in addition to provision of LICIAcube imaging data.

Competing interests The authors declare no competing interests.

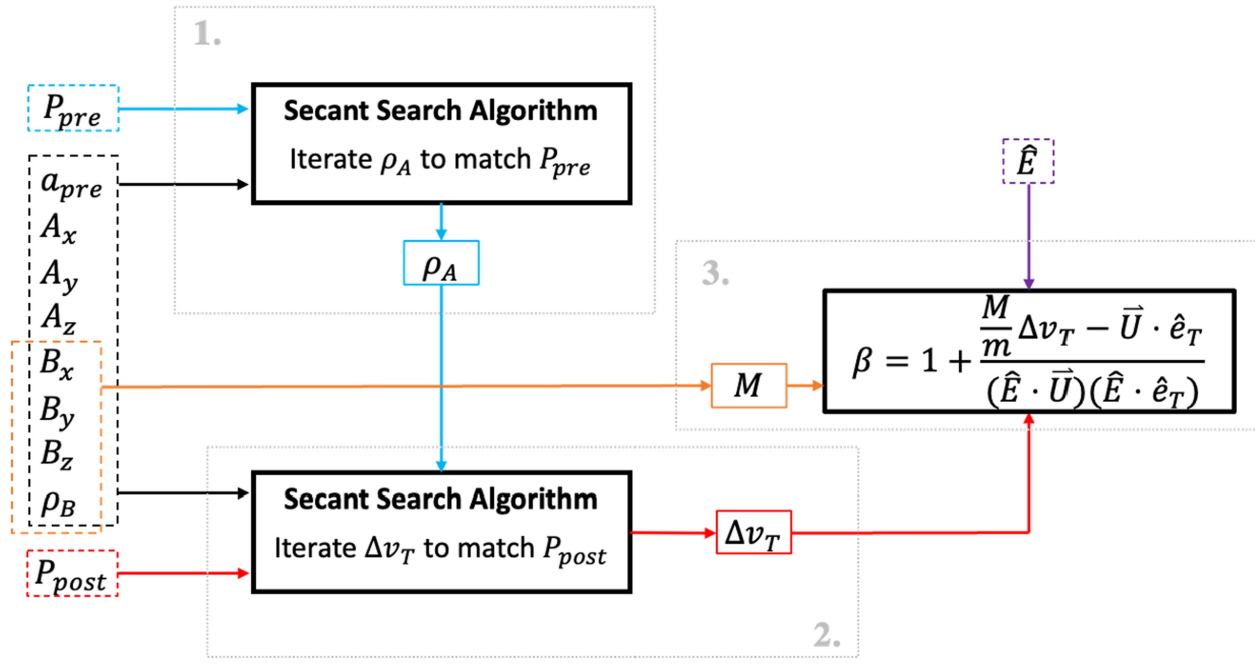
Additional information

Supplementary information The online version contains supplementary material available at <https://doi.org/10.1038/s41586-023-05878-z>.

Correspondence and requests for materials should be addressed to Andrew F. Cheng.

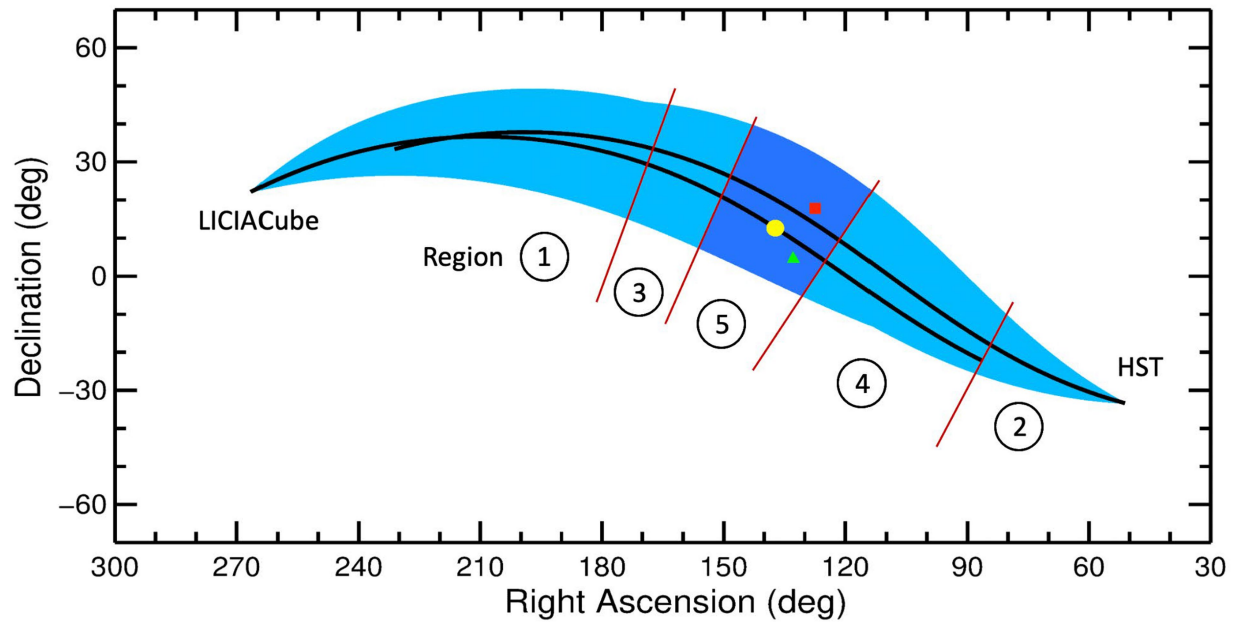
Peer review information Nature thanks the anonymous reviewer(s) for their contribution to the peer review of this work. Peer reviewer reports are available.

Reprints and permissions information is available at <http://www.nature.com/reprints>.



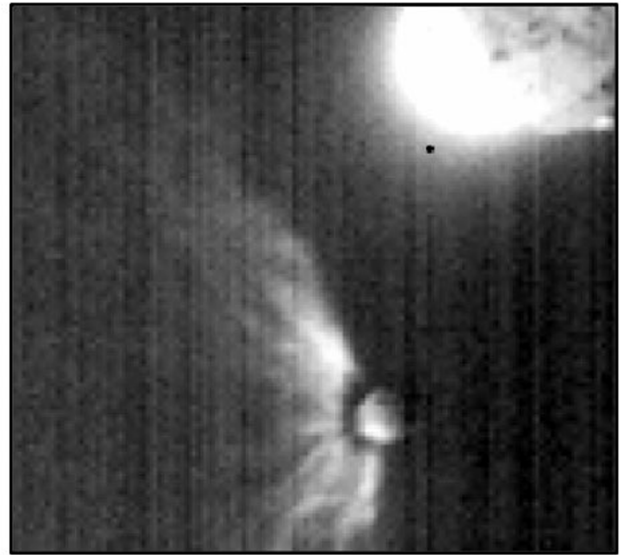
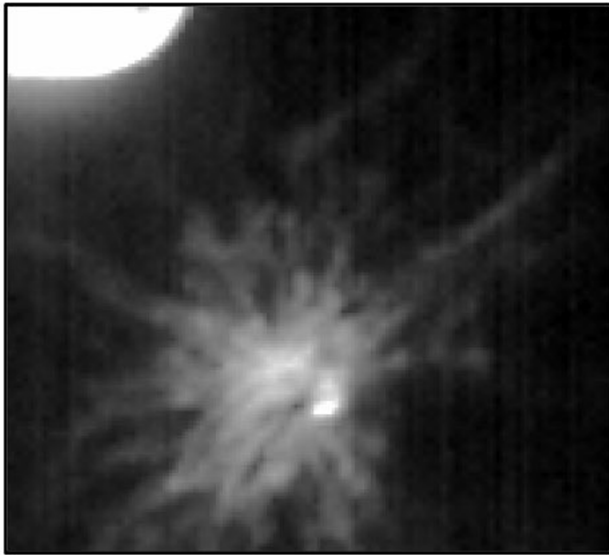
Extended Data Fig. 1 | Outline of algorithm used to calculate β . The Monte Carlo variables are outlined by dashed lines and are defined as follows: pre-impact orbit period P_{pre} ; pre-impact orbit semimajor axis a_{pre} ; Didymos ellipsoid extents A_x, A_y, A_z ; Dimorphos ellipsoid extents B_x, B_y, B_z ; Dimorphos density ρ_B ; post-impact orbit period P_{post} ; and net ejecta momentum direction \hat{E} . First,

a secant algorithm iterates Didymos density ρ_A to match P_{pre} . Next, another secant algorithm iterates the along-track change in Dimorphos's velocity Δv_T to match P_{post} . Finally, M is calculated using the ellipsoid extents and density of Dimorphos, and then combined with Δv_T and \hat{E} to calculate β .



Extended Data Fig. 2 | Ejecta cone orientation lies in the swaths of sky (black lines) defined by HST and LICIACube observations. The light-blue envelope outlines the axis position uncertainty in the direction measured in the sky plane. Red lines divide the along-plane swaths into regions that are excluded based on cone morphology in LICIACube images: 1) and 2) are excluded because the ejecta cone would point in the opposite direction from what is observed; 3) is excluded because the axis would lie too close to the sky plane; 4)

is excluded because the axis would lie too close to the line-of-sight; and 5) is the expected region for the axis orientation. The yellow dot denotes the best solution (RA, Dec) = [138°, +13°] with the dark-blue envelope showing the extent of possible solutions. The red square is the direction of the incoming DART trajectory [128°, +18°] and the green triangle shows Dimorphos's velocity vector [134°, +5°]. The LICIACube swath is defined for the +175s image shown in Extended Data Fig. 3.



Extended Data Fig. 3 | Two LICIACube LUKE images showing the ejecta morphology that were used to reduce the possible axis orientation solutions. The left panel shows an approach observation, 156 s after impact, with the ejecta in front of and partially obscuring Dimorphos. The right panel shows the ejecta morphology after close approach, 175 s after impact, with

Dimorphos silhouetted against the ejecta cone. The images show the red channel from frames LICIACUBE_LUKE_L2_1664234220_00005_01 and LICIACUBE_LUKE_L2_1664234239_01003_01. The bright object in the upper corner of each image is Didymos.

Extended Data Table 1 | Values and uncertainties used for numerical simulations

Quantity	Value	Uncertainty Assumed in Monte Carlo simulations	Note
DART mass at impact, m [kg]	579.4	Not considered	Actual uncertainty ¹ ± 0.7
DART incident velocity vector x [km/s], \vec{U}_x	3.57399	Not considered	See Data Availability for source information.
DART incident velocity vector y [km/s], \vec{U}_y	-4.64106	Not considered	See Data Availability for source information.
DART incident velocity vector z [km/s], \vec{U}_z	-1.85622	Not considered	See Data Availability for source information.
Orbit period pre-impact, P_{pre} [hr]	11.92148	± 0.00044	1σ , Gaussian, reported by the “N22+” solution in ref. ²
Orbit period post-impact, P_{post} [hr]	11.372	± 0.0055	1σ , Gaussian, reported by the “N22+” solution in ref. ²
Pre-impact orbit separation (semi-major axis), a_{pre} [km]	1.206	± 0.035	1σ , Gaussian, reported by the “N22+” solution in ref. ²
Didymos major axis, A_x [m]	851	± 15	sampled uniformly ¹
Didymos intermediate axis, A_y [m]	849	± 15	sampled uniformly ¹
Didymos minor axis, A_z [m]	620	± 15	sampled uniformly ¹
Dimorphos major axis, B_x [m]	177	± 2	sampled uniformly ¹
Dimorphos intermediate axis, B_y [m]	174	± 4	sampled uniformly ¹
Dimorphos minor axis, B_z [m]	116	± 2	sampled uniformly ¹
Dimorphos density, ρ_B [kg m ⁻³]	2400	± 900	Sampled uniformly. Three times the density uncertainty on the combined Didymos system from ref. ¹
Ejecta cone direction x, \hat{E}_x	-0.72410	Uncertainty is within a 15° cone around this nominal vector	Sample uniformly throughout a cone of directions up to 15° away nominal RA,Dec = 138°, +13°
Ejecta cone direction y, \hat{E}_y	0.65198		
Ejecta cone direction z, \hat{E}_z	0.22495		
Dimorphos orbital velocity direction x, \hat{e}_{T_x}	-0.689282	Not considered	See Data Availability for source information.
Dimorphos orbital velocity direction y, \hat{e}_{T_y}	0.716645	Not considered	See Data Availability for source information.
Dimorphos orbital velocity direction z, \hat{e}_{T_z}	0.106350	Not considered	See Data Availability for source information.

All vectors are reported in the Earth Mean Equator J2000 (EME J2000) coordinate frame, at the impact time of September 26, 2022, 23:14:24.183 UTC¹. For Gaussian uncertainties we report the 1σ uncertainties. For uniform uncertainties we report the median and the range of possible values.

Extended Data Table 2 | Covariance matrix

	a_{pre}	n_{pre}	Δn
a_{pre}	1.23278161e-03	-5.07112880e-12	7.08461748e-10
n_{pre}	-5.07112880e-12	2.90452780e-19	-2.31470184e-17
Δn	7.08461748e-10	-2.31470184e-17	4.94295884e-15

The covariances used to sample semimajor axis, a_{pre} , and pre- and post-impact orbit periods. The orbital solution from refs. 2,36 fits the pre-impact mean motion at the impact epoch, n_{pre} and the change in mean motion due to the DART impact, Δn . Once these parameters are sampled, they are turned into a pre- and post-impact orbit period by the relation $P_{pre} = 2\pi/n_{pre}$ and $P_{post} = 2\pi/(n_{pre} + \Delta n)$. The covariance matrix is constructed using units of km for a_{pre} and rad/s for n_{pre} and Δn .